

# Resonances in axially symmetric dielectric objects

Johan Helsing\* and Anders Karlsson†

February 28, 2022

## Abstract

A high-order convergent and robust numerical solver is constructed and used to find complex eigenwavenumbers and electromagnetic eigenfields of dielectric objects with axial symmetry. The solver is based on Fourier–Nyström discretization of combined integral equations for the transmission problem and can be applied to demanding resonance problems at microwave, terahertz, and optical wavelengths. High achievable accuracy, even at very high wavenumbers, makes the solver ideal for benchmarking and for assessing the performance of general purpose commercial software.

## 1 Introduction

This paper is about the fundamental problem of determining resonances of axially symmetric homogeneous dielectric objects in vacuum. The problem is formulated as an eigenvalue problem based on a combination of the electric field integral equation (EFIE), the magnetic field integral equation (MFIE), and two charge integral equations (ChIEs). It is solved numerically using a high-order convergent discretization scheme. A motivation for this work is to be able to produce very accurate evaluations that can serve as benchmark tests for other methods. This aim has lead us to use a formulation that, with our scheme, gives the most accurate evaluations.

In microwave technology dielectric resonators are interesting since they are cost effective and lead to significant miniaturization, particularly of microwave integrated circuits. They give excellent performance to antennas [1] and filters [2]. A nice review of dielectric resonators in microwave technology is given in [3]. Resonant dielectric objects also play an important role in the recent progress in nano-optics. A good example is axially symmetric structures that exhibit whispering gallery modes (WGMs) [4]. WGMs have large Q-factors (commercial micro-optical WGM resonators can have  $Q > 10^8$ ) and their eigenfields are confined to a small volume in the outer

---

\*Centre for Mathematical Sciences, Lund University, Sweden

†Electrical and Information Technology, Lund University, Sweden

part of the dielectric object. These properties are very useful in the design of microcavity lasers [5] and extremely sensitive sensors [6] and for the generation of frequency combs [7, 8]. WGMs have been used for determining electric properties of materials [9] at microwave frequencies, but otherwise WGMs have been less exploited in microwave technology than in optics.

Common numerical methods for the determination of electromagnetic resonances in dielectric objects include the finite element method (FEM) [10], boundary integral equation (BIE) methods [11, 12, 13], the discrete dipole approximation (DDA) method [14], and the null-field method [15]. The method used in the present paper belongs to the category of BIE methods, which comprise a variety of formulations and techniques. In [16] the integral equations derived by Müller [17, Section 23] was applied to scattering from dielectric objects. We use a related set of integral equations and a modification of the Fourier–Nyström scheme of [13], which in turn draws on progress in [12, 18, 19, 20, 21].

Most BIE methods for transmission problems use the electric and magnetic surface current densities as unknowns. A particular feature of the present work is that we also let the surface charge densities be unknowns. There are two reasons for this: First, the problem of evaluating compact differences of hypersingular operators in the classical Müller formulation is avoided. Second, numerical differentiation of surface currents for the evaluation of eigenfields is avoided. As a result, our scheme can be made higher-order and attain extraordinary accuracy. It can easily solve resonance problems that, to our knowledge, previously have been essentially inaccessible.

We remark that the use of unknown surface charge densities to improve the performance of numerical schemes is not new. It was introduced as a way to overcome the, so called, low frequency breakdown problem of BIE methods in [22] and was further developed for this purpose in [23]. See also [24, Appendix A]. In [12] and [13] it was recognized that the use of unknown surface charges is numerically favorable also at higher frequencies.

The paper is organized as follows: Section 2 describes the geometry and formulates our problem in terms of partial differential equations (PDEs). Section 3 introduces integral representations of electric and magnetic fields in terms of surface densities, derives the integral equations and discusses their relation to the Müller integral equations. Section 4 restricts the analysis to axially symmetric objects. Fourier series expansions are used to express the homogeneous system of integral equations, from which wavenumbers and surface densities representing eigenfields are obtained, in a form that is well-suited for discretization. Section 5 defines useful physical quantities and relate them to the surface densities. The numerical method is described in Section 6. Some challenging numerical examples, involving various types of resonant modes, are given in Section 7.

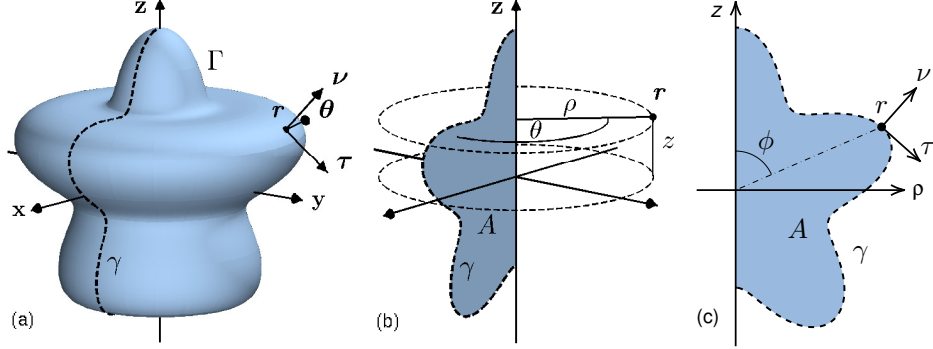


Figure 1: The geometry described in  $\mathbb{R}^3$  and in  $\mathbb{R}^2$ . (a) The outward unit normal  $\nu$  and tangent vector  $\tau$  at a point  $r$  on  $\Gamma$ . The volume outside  $\Gamma$  is  $V_1$  and the volume inside is  $V_2$ . (b) The radial distance  $\rho$ , azimuthal angle  $\theta$ , and height  $z$  of a point  $r$ . The domain  $A$  and the generating curve  $\gamma$ . (c) The half-plane  $\mathbb{H}$  with two-dimensional vectors.

## 2 Problem formulation

### 2.1 Geometry

The notation is the same as in [13]. In particular,  $\Gamma$  is an axially symmetric surface enclosing a body of revolution  $V_2$  in  $\mathbb{R}^3$ , the unbounded exterior to  $\Gamma$  is  $V_1$ ,

$$\mathbf{r} = \hat{\mathbf{r}}|\mathbf{r}| = (x, y, z) = (\rho \cos \theta, \rho \sin \theta, z) \quad (1)$$

is a point in  $\mathbb{R}^3$ ,  $\theta$  is the azimuthal angle,  $\rho = \sqrt{x^2 + y^2}$ , and  $\hat{\mathbf{r}}$  is the radial unit vector. The outward unit normal  $\nu$  on  $\Gamma$  is

$$\nu = (\nu_\rho \cos \theta, \nu_\rho \sin \theta, \nu_z) \quad (2)$$

and

$$\begin{aligned} \rho &= (\cos \theta, \sin \theta, 0), \\ \theta &= (-\sin \theta, \cos \theta, 0), \\ \tau &= (\nu_z \cos \theta, \nu_z \sin \theta, -\nu_\rho), \\ z &= (0, 0, 1), \end{aligned} \quad (3)$$

are other unit vectors. See Figure 1(a) and 1(b).

The angle  $\theta = 0$  defines a half-plane  $\mathbb{H}$  in  $\mathbb{R}^3$ . The intersection of  $\mathbb{H}$  and  $\Gamma$  is the generating curve  $\gamma$ , points in  $\mathbb{H}$  are denoted  $r = (\rho, z)$ , the planar domain bounded by  $\gamma$  and the  $z$ -axis is  $A$ , the outward unit normal on  $\gamma$  is  $\nu = (\nu_\rho, \nu_z)$ , and  $\tau = (\nu_z, -\nu_\rho)$  is a tangent. See Figure 1(c).

## 2.2 PDE-formulation

The domain  $V_2$  is a homogeneous dielectric object with constant complex refractive index  $m$ . In  $V_1$  there is vacuum. The electric field is everywhere scaled with the free space wave impedance  $\eta_0$  such that  $\mathbf{E} = \eta_0^{-1} \mathbf{E}_{\text{unsc}}$ , where  $\mathbf{E}_{\text{unsc}}$  is the unscaled field. Then  $\mathbf{E}$  and the magnetic field  $\mathbf{H}$  have the same dimensions.

Sources can be located in a bounded volume  $V_{s1}$  in  $V_1$  and  $V_{s2}$  in  $V_2$  and generate time harmonic incident fields with complex electric and magnetic fields  $\mathbf{E}_1^{\text{inc}}, \mathbf{H}_1^{\text{inc}}$  in  $V_1$  and  $\mathbf{E}_2^{\text{inc}}, \mathbf{H}_2^{\text{inc}}$  in  $V_2$ . These give rise to the scattered fields  $\mathbf{E}^{\text{sca}}$  and  $\mathbf{H}^{\text{sca}}$  in  $V_1$  and  $V_2$ . We prefer to work with the total electric and magnetic fields  $\mathbf{E}$  and  $\mathbf{H}$ , which are the sum of the incident and scattered fields. From the Maxwell equations it follows that the total fields satisfy the system of PDEs

$$\nabla \times \mathbf{E}(\mathbf{r}) = ik_j \mathbf{H}(\mathbf{r}), \quad \mathbf{r} \in V_j \setminus V_{sj}, \quad j = 1, 2, \quad (4)$$

$$\nabla \times \mathbf{H}(\mathbf{r}) = -ik_j \mathbf{E}(\mathbf{r}), \quad \mathbf{r} \in V_j \setminus V_{sj}, \quad j = 1, 2, \quad (5)$$

$$k_2 = mk_1, \quad (6)$$

where  $k_1 = \omega/c$  and  $k_2$  are the wavenumbers in  $V_1$  and  $V_2$ ,  $\omega$  is the angular frequency, and  $c$  is the speed of light in vacuum. We use the time dependence  $e^{-i\omega t}$ . Then  $\Im m\{m\} > 0$ , since the material in  $V_2$  is assumed to be passive. From now on we will, for the most part, omit the subscript of  $k_1$  and write the (vacuum) wavenumber in  $V_1$  as  $k$ .

The boundary conditions on  $\Gamma$  are

$$\lim_{V_1 \ni \mathbf{r} \rightarrow \mathbf{r}^\circ} \boldsymbol{\nu}^\circ \cdot \mathbf{E}(\mathbf{r}) = \lim_{V_2 \ni \mathbf{r} \rightarrow \mathbf{r}^\circ} m^2 \boldsymbol{\nu}^\circ \cdot \mathbf{E}(\mathbf{r}), \quad \mathbf{r}^\circ \in \Gamma, \quad (7)$$

$$\lim_{V_1 \ni \mathbf{r} \rightarrow \mathbf{r}^\circ} \boldsymbol{\nu}^\circ \times \mathbf{E}(\mathbf{r}) = \lim_{V_2 \ni \mathbf{r} \rightarrow \mathbf{r}^\circ} \boldsymbol{\nu}^\circ \times \mathbf{E}(\mathbf{r}), \quad \mathbf{r}^\circ \in \Gamma, \quad (8)$$

$$\lim_{V_1 \ni \mathbf{r} \rightarrow \mathbf{r}^\circ} \boldsymbol{\nu}^\circ \times \mathbf{H}(\mathbf{r}) = \lim_{V_2 \ni \mathbf{r} \rightarrow \mathbf{r}^\circ} \boldsymbol{\nu}^\circ \times \mathbf{H}(\mathbf{r}), \quad \mathbf{r}^\circ \in \Gamma, \quad (9)$$

$$\lim_{V_1 \ni \mathbf{r} \rightarrow \mathbf{r}^\circ} \boldsymbol{\nu}^\circ \cdot \mathbf{H}(\mathbf{r}) = \lim_{V_2 \ni \mathbf{r} \rightarrow \mathbf{r}^\circ} \boldsymbol{\nu}^\circ \cdot \mathbf{H}(\mathbf{r}), \quad \mathbf{r}^\circ \in \Gamma, \quad (10)$$

and the radiation condition for the scattered field in  $V_1$  is

$$\begin{aligned} \mathbf{E}^{\text{sca}}(\mathbf{r}) &= \frac{e^{ik|\mathbf{r}|}}{|\mathbf{r}|} \left( \mathbf{F}(\hat{\mathbf{r}}) + \mathcal{O}\left(\frac{1}{|\mathbf{r}|}\right) \right), \quad |\mathbf{r}| \rightarrow \infty, \\ \mathbf{H}^{\text{sca}}(\mathbf{r}) &= \frac{e^{ik|\mathbf{r}|}}{|\mathbf{r}|} \left( \hat{\mathbf{r}} \times \mathbf{F}(\hat{\mathbf{r}}) + \mathcal{O}\left(\frac{1}{|\mathbf{r}|}\right) \right), \quad |\mathbf{r}| \rightarrow \infty, \end{aligned} \quad (11)$$

where  $\mathbf{F}$  is the electric far-field pattern, see [25, Eq. (6.23)].

Our resonance problem can now be formulated as follows: we seek non-trivial solutions to (4)-(11) when the incident fields are zero. The solutions are the eigenwavenumbers  $k$  and the eigenfields  $\mathbf{E}$  and  $\mathbf{H}$ .

### 2.3 The radiation condition at complex wavenumbers

We shall solve (4)-(11) using a BIE method where the integral equations are derived from integral representations of  $\mathbf{E}$  and  $\mathbf{H}$  containing the Green's function

$$\Phi_k(\mathbf{r}, \mathbf{r}') = \frac{e^{ik|\mathbf{r}-\mathbf{r}'|}}{4\pi|\mathbf{r}-\mathbf{r}'|}. \quad (12)$$

The radiation condition (11) is then automatically satisfied and says that, for real  $k$  and in the far zone, the scattered field is an outward traveling spherical vector wave.

At resonances, the eigenwavenumbers  $k$  are complex with negative imaginary part. The condition (11) then says that the eigenfields grow exponentially at large distances. This is required for the fields to satisfy causality and for the corresponding time domain fields to be exponentially decaying as  $e^{\Im\{k\}ct}$  in time. Causality says that the fields of a resonance at a time  $t$  and at a distance  $|\mathbf{r}|$  from an object left the object at time  $t - |\mathbf{r}|/c$ . The attenuation implies that at time  $t - |\mathbf{r}|/c$ , the fields in the object were  $e^{-\Im\{k\}r}$  times stronger than at time  $t$ , in accordance with (11).

The condition (11) is vital in the derivation of integral representations of  $\mathbf{E}$  and  $\mathbf{H}$  in  $V_1$ . In [26, Section IIC] it is shown that such derivations hold also for eigenfields with complex eigenwavenumbers, despite their exponential growth in the radial direction.

## 3 Integral representations and equations

This section gives integral representations of  $\mathbf{E}$  and  $\mathbf{H}$  along with our system of BIEs for a general three-dimensional dielectric object. The integral representations use four fictitious surface densities on  $\Gamma$ : the magnetic and electric surface current densities  $\mathbf{M}_s$  and  $\mathbf{J}_s$ , and the electric and magnetic surface charge densities  $\varrho_E$  and  $\varrho_M$ . The system of BIEs contains the EFIE, the MFIE, the electric ChIE (EChIE), and the magnetic ChIE (MChIE).

### 3.1 Surface densities and integral representations

The densities  $\mathbf{M}_s$ ,  $\mathbf{J}_s$ ,  $\varrho_E$ , and  $\varrho_M$  are defined from a viewpoint in  $V_1$ . With  $\mathbf{r}^\circ \in \Gamma$ :

$$\varrho_E(\mathbf{r}^\circ) \equiv \lim_{V_1 \ni \mathbf{r} \rightarrow \mathbf{r}^\circ} \boldsymbol{\nu}^\circ \cdot \mathbf{E}(\mathbf{r}) = \lim_{V_2 \ni \mathbf{r} \rightarrow \mathbf{r}^\circ} m^2 \boldsymbol{\nu}^\circ \cdot \mathbf{E}(\mathbf{r}) \quad (13)$$

$$\mathbf{M}_s(\mathbf{r}^\circ) \equiv \lim_{V_1 \ni \mathbf{r} \rightarrow \mathbf{r}^\circ} \mathbf{E}(\mathbf{r}) \times \boldsymbol{\nu}^\circ = \lim_{V_2 \ni \mathbf{r} \rightarrow \mathbf{r}^\circ} \mathbf{E}(\mathbf{r}) \times \boldsymbol{\nu}^\circ \quad (14)$$

$$\mathbf{J}_s(\mathbf{r}^\circ) \equiv \lim_{V_1 \ni \mathbf{r} \rightarrow \mathbf{r}^\circ} \boldsymbol{\nu}^\circ \times \mathbf{H}(\mathbf{r}) = \lim_{V_2 \ni \mathbf{r} \rightarrow \mathbf{r}^\circ} \boldsymbol{\nu}^\circ \times \mathbf{H}(\mathbf{r}) \quad (15)$$

$$\varrho_M(\mathbf{r}^\circ) \equiv \lim_{V_1 \ni \mathbf{r} \rightarrow \mathbf{r}^\circ} \boldsymbol{\nu}^\circ \cdot \mathbf{H}(\mathbf{r}) = \lim_{V_2 \ni \mathbf{r} \rightarrow \mathbf{r}^\circ} \boldsymbol{\nu}^\circ \cdot \mathbf{H}(\mathbf{r}). \quad (16)$$

The second equalities in (13)-(16) hold when the boundary conditions (7)-(10) are met.

Our integral representations of  $\mathbf{E}(\mathbf{r})$  and  $\mathbf{H}(\mathbf{r})$  are for  $\mathbf{r} \in V_1$

$$\begin{aligned}\mathbf{E}(\mathbf{r}) &= \mathbf{E}_1^{\text{inc}}(\mathbf{r}) - \mathcal{N}\varrho_E(\mathbf{r}) - \mathcal{K}\mathbf{M}_s(\mathbf{r}) + ik\mathcal{S}\mathbf{J}_s(\mathbf{r}), \\ \mathbf{H}(\mathbf{r}) &= \mathbf{H}_1^{\text{inc}}(\mathbf{r}) + ik\mathcal{S}\mathbf{M}_s(\mathbf{r}) + \mathcal{K}\mathbf{J}_s(\mathbf{r}) - \mathcal{N}\varrho_M(\mathbf{r}),\end{aligned}\tag{17}$$

and for  $\mathbf{r} \in V_2$

$$\begin{aligned}\mathbf{E}(\mathbf{r}) &= \mathbf{E}_2^{\text{inc}}(\mathbf{r}) + m^{-2}\tilde{\mathcal{N}}\varrho_E(\mathbf{r}) + \tilde{\mathcal{K}}\mathbf{M}_s(\mathbf{r}) - ik\tilde{\mathcal{S}}\mathbf{J}_s(\mathbf{r}), \\ \mathbf{H}(\mathbf{r}) &= \mathbf{H}_2^{\text{inc}}(\mathbf{r}) - im^2k\tilde{\mathcal{S}}\mathbf{M}_s(\mathbf{r}) - \tilde{\mathcal{K}}\mathbf{J}_s(\mathbf{r}) + \tilde{\mathcal{N}}\varrho_M(\mathbf{r}),\end{aligned}\tag{18}$$

where the integral operators  $\mathcal{S}$ ,  $\mathcal{N}$ , and  $\mathcal{K}$  are defined by their actions on scalar or vector surface densities  $g(\mathbf{r})$  and  $\mathbf{g}(\mathbf{r})$  as

$$\mathcal{S}g(\mathbf{r}) = \int_{\Gamma} \Phi_k(\mathbf{r}, \mathbf{r}')g(\mathbf{r}') d\Gamma',\tag{19}$$

$$\mathcal{N}g(\mathbf{r}) = \int_{\Gamma} \nabla\Phi_k(\mathbf{r}, \mathbf{r}')g(\mathbf{r}') d\Gamma',\tag{20}$$

$$\mathcal{K}\mathbf{g}(\mathbf{r}) = \int_{\Gamma} \nabla\Phi_k(\mathbf{r}, \mathbf{r}') \times \mathbf{g}(\mathbf{r}') d\Gamma',\tag{21}$$

and  $\tilde{\mathcal{S}}$ ,  $\tilde{\mathcal{N}}$ , and  $\tilde{\mathcal{K}}$  are defined analogously, but with  $\Phi_k$  replaced by  $\Phi_{k_2}$ .

### 3.2 Integral equations

We now form a system of BIE on  $\Gamma$ . It comes from using (17) and (18) in the definitions (13)-(16) and taking the limits  $\mathbf{r} \rightarrow \mathbf{r}^\circ \in \Gamma$ . Each definition gives rise to two BIEs: one for  $\mathbf{r} \in V_1$  and one for  $\mathbf{r} \in V_2$ .

The BIEs coming from  $\mathbf{r} \in V_1$  are

$$\begin{aligned}\varrho_E + 2\boldsymbol{\nu} \cdot (\mathcal{N}\varrho_E + \mathcal{K}\mathbf{M}_s - ik\mathcal{S}\mathbf{J}_s) &= 2\boldsymbol{\nu} \cdot \mathbf{E}_1^{\text{inc}}, \\ \mathbf{M}_s - 2\boldsymbol{\nu} \times (\mathcal{N}\varrho_E + \mathcal{K}\mathbf{M}_s - ik\mathcal{S}\mathbf{J}_s) &= -2\boldsymbol{\nu} \times \mathbf{E}_1^{\text{inc}}, \\ \mathbf{J}_s - 2\boldsymbol{\nu} \times (ik\mathcal{S}\mathbf{M}_s + \mathcal{K}\mathbf{J}_s - \mathcal{N}\varrho_M) &= 2\boldsymbol{\nu} \times \mathbf{H}_1^{\text{inc}}, \\ \varrho_M - 2\boldsymbol{\nu} \cdot (ik\mathcal{S}\mathbf{M}_s + \mathcal{K}\mathbf{J}_s - \mathcal{N}\varrho_M) &= 2\boldsymbol{\nu} \cdot \mathbf{H}_1^{\text{inc}}.\end{aligned}\tag{22}$$

The BIEs coming from  $\mathbf{r} \in V_2$  are

$$\begin{aligned}\varrho_E - 2\boldsymbol{\nu} \cdot (\tilde{\mathcal{N}}\varrho_E + m^2\tilde{\mathcal{K}}\mathbf{M}_s - im^2k\tilde{\mathcal{S}}\mathbf{J}_s) &= 2m^2\boldsymbol{\nu} \cdot \mathbf{E}_2^{\text{inc}}, \\ \mathbf{M}_s + 2\boldsymbol{\nu} \times (m^{-2}\tilde{\mathcal{N}}\varrho_E + \tilde{\mathcal{K}}\mathbf{M}_s - ik\tilde{\mathcal{S}}\mathbf{J}_s) &= -2\boldsymbol{\nu} \times \mathbf{E}_2^{\text{inc}}, \\ \mathbf{J}_s + 2\boldsymbol{\nu} \times (im^2k\tilde{\mathcal{S}}\mathbf{M}_s + \tilde{\mathcal{K}}\mathbf{J}_s - \tilde{\mathcal{N}}\varrho_M) &= 2\boldsymbol{\nu} \times \mathbf{H}_2^{\text{inc}}, \\ \varrho_M + 2\boldsymbol{\nu} \cdot (im^2k\tilde{\mathcal{S}}\mathbf{M}_s + \tilde{\mathcal{K}}\mathbf{J}_s - \tilde{\mathcal{N}}\varrho_M) &= 2\boldsymbol{\nu} \cdot \mathbf{H}_2^{\text{inc}}.\end{aligned}\tag{23}$$

The order of the equations in (22) and (23) is from top to bottom: EChIE, EFIE, MFIE, and MChIE.

We collect the systems (22) and (23) in block operator form

$$\mathbf{Q}_1 \boldsymbol{\sigma} = \mathbf{f}_1, \quad (24)$$

$$\mathbf{Q}_2 \boldsymbol{\sigma} = \mathbf{f}_2, \quad (25)$$

where

$$\boldsymbol{\sigma} = \begin{bmatrix} \varrho_E \\ \mathbf{M}_s \\ \mathbf{J}_s \\ \varrho_M \end{bmatrix}, \quad \mathbf{f}_1 = 2 \begin{bmatrix} \boldsymbol{\nu} \cdot \mathbf{E}_1^{\text{inc}} \\ -\boldsymbol{\nu} \times \mathbf{E}_1^{\text{inc}} \\ \boldsymbol{\nu} \times \mathbf{H}_1^{\text{inc}} \\ \boldsymbol{\nu} \cdot \mathbf{H}_1^{\text{inc}} \end{bmatrix}, \quad \mathbf{f}_2 = 2 \begin{bmatrix} m^2 \boldsymbol{\nu} \cdot \mathbf{E}_2^{\text{inc}} \\ -\boldsymbol{\nu} \times \mathbf{E}_2^{\text{inc}} \\ \boldsymbol{\nu} \times \mathbf{H}_2^{\text{inc}} \\ \boldsymbol{\nu} \cdot \mathbf{H}_2^{\text{inc}} \end{bmatrix}, \quad (26)$$

and where  $\mathbf{Q}_1$  and  $\mathbf{Q}_2$  are square block operator matrices. The system (24) is, modulo normalization constants, identical to [22, Eq. 18]. Our resonance problem means that we must find simultaneous nontrivial solutions to (24) and (25) when  $\mathbf{f}_1 = \mathbf{f}_2 = \mathbf{0}$ .

### 3.3 The ChIE-extended formulation and its relation to the Müller BIE

We adopt a combination of (24) and (25) that we refer to as the ChIE extended formulation since it contains the electric and magnetic surface charge densities as unknowns.

$$(\mathbf{Q}_1 + \mathbf{Q}_2) \boldsymbol{\sigma} = \mathbf{f}_1 + \mathbf{f}_2, \quad (27)$$

In Section 7 we make a comparison between a scheme based on (27) and a scheme based on the combination of BIE presented by Müller in [17, p. 319]. The Müller combination is

$$\mathbf{Q}_3 \boldsymbol{\sigma}_M = \mathbf{f}_M, \quad (28)$$

where

$$\boldsymbol{\sigma}_M = \begin{bmatrix} \mathbf{M}_s \\ \mathbf{J}_s \end{bmatrix} \quad (29)$$

and

$$\mathbf{f}_M = 2 \begin{bmatrix} -\boldsymbol{\nu} \times (\mathbf{E}_1^{\text{inc}} + m^2 \mathbf{E}_2^{\text{inc}}) \\ \boldsymbol{\nu} \times (\mathbf{H}_1^{\text{inc}} + \mathbf{H}_2^{\text{inc}}) \end{bmatrix}. \quad (30)$$

In accordance with [16], we refer to it as the classical Müller combination. It can be modified to a version that often is preferred for method of moment schemes

$$\mathbf{Q}_4 \boldsymbol{\sigma}_M = \mathbf{f}_M. \quad (31)$$

The matrix operators in (28) and (31) are

$$\mathbf{Q}_3 = \begin{bmatrix} (1 + m^2)I - 2\boldsymbol{\nu} \times (\mathcal{K} - m^2\tilde{\mathcal{K}}) & 2ik\boldsymbol{\nu} \times (\mathcal{S} - m^2\tilde{\mathcal{S}} + k^{-2}(\mathcal{L} - \tilde{\mathcal{L}})) \\ -2ik\boldsymbol{\nu} \times (\mathcal{S} - m^2\tilde{\mathcal{S}} + k^{-2}(\mathcal{L} - \tilde{\mathcal{L}})) & 2I - 2\boldsymbol{\nu} \times (\mathcal{K} - \tilde{\mathcal{K}}) \end{bmatrix} \quad (32)$$

$$\mathbf{Q}_4 = \begin{bmatrix} (1 + m^2)I - 2\boldsymbol{\nu} \times (\mathcal{K} - m^2\tilde{\mathcal{K}}) & 2ik\boldsymbol{\nu} \times (\mathcal{S} - m^2\tilde{\mathcal{S}} + k^{-2}(\mathcal{P} - \tilde{\mathcal{P}})) \\ -2ik\boldsymbol{\nu} \times (\mathcal{S} - m^2\tilde{\mathcal{S}} + k^{-2}(\mathcal{P} - \tilde{\mathcal{P}})) & 2I - 2\boldsymbol{\nu} \times (\mathcal{K} - \tilde{\mathcal{K}}) \end{bmatrix} \quad (33)$$

where

$$\begin{aligned} \mathcal{L}\mathbf{g}(\mathbf{r}) &= \nabla \int_{\Gamma} (\nabla \Phi_k(\mathbf{r}, \mathbf{r}') \cdot \mathbf{g}(\mathbf{r}') d\Gamma' \\ \mathcal{P}\mathbf{g}(\mathbf{r}) &= \int_{\Gamma} \nabla \Phi_k(\mathbf{r}, \mathbf{r}') \nabla' \cdot \mathbf{g}(\mathbf{r}') d\Gamma' \end{aligned} \quad (34)$$

The combinations (31) and (27) are related via

$$\varrho_E(\mathbf{r}) = -\frac{i}{k} \nabla_s \cdot \mathbf{J}_s(\mathbf{r}), \quad (35)$$

$$\varrho_M(\mathbf{r}) = -\frac{i}{k} \nabla_s \cdot \mathbf{M}_s(\mathbf{r}), \quad (36)$$

where  $\nabla_s \cdot ()$  is the surface divergence.

The operators  $\mathcal{L}$  and  $\tilde{\mathcal{L}}$  in (28) are hypersingular, but the hypersingularities cancel out in the difference  $\mathcal{L} - \tilde{\mathcal{L}}$ . By that (28) becomes a system of Fredholm second kind integral equations with compact integral operators [17, p. 300]. The hypersingularities are still present in the integral representations of the electric and magnetic fields and need to be handled by care in the evaluation of the fields close to  $\Gamma$ . It is not straightforward to implement (28). This is one reason why (31), which does not contain hypersingular operators, is an alternative. Our versions of  $\mathbf{Q}_1$  and  $\mathbf{Q}_2$  are free from hypersingular integral operators but they do contain singular operators defined only in the sense of the Cauchy principal value and do not all cancel out in the sum  $\mathbf{Q}_1 + \mathbf{Q}_2$ .

Müller showed two additional properties of his classical formulation under the condition that  $\Gamma$  consists of only one closed regular surface:

1. The system (28) has a unique solution  $\boldsymbol{\sigma}$  for wavenumbers  $k$  with  $0 \leq \arg\{k\} < \pi$  and  $0 \leq \arg\{m^2\} < \pi/2$ , [17, Theorem 68].
2. With  $\boldsymbol{\sigma}$  as the unique solution to (28), the corresponding fields  $\mathbf{E}$  and  $\mathbf{H}$  obtained from (17) and (18) are solutions to the Maxwell equations [17, Theorem 69]. By that they also satisfy (4)-(11).

A conjecture is that the ChIE-extended formulation (27) also has these properties. Furthermore, in our numerical experiments with  $\mathbf{f}_1 = \mathbf{f}_2 = \mathbf{0}$

we check that all nontrivial solutions to (27) also solve (24) and (25) to the same precision and that (35) and (36) hold (with a few digits lost in the numerical differentiation). We have not been able to detect any solution to (27) that violates these tests.

### 3.4 Physical resonances

Our goal is to find eigenwavenumbers  $k$  for the homogeneous version of (27)

$$(\mathbf{Q}_1 + \mathbf{Q}_2)\boldsymbol{\sigma} = \mathbf{0} \quad (37)$$

and to evaluate their corresponding eigenfields  $\mathbf{E}$  and  $\mathbf{H}$  from (17) and (18) via  $\boldsymbol{\sigma}$ . The eigenwavenumbers have  $\Im\{k\} < 0$  and constitute an infinite countable set.

## 4 Axial symmetry

So far our analysis is valid for arbitrary dielectric objects. We now restrict it to objects with axial symmetry and perform an azimuthal Fourier transformation of (24) and (25) and of (17) and (18) to obtain modal integral equations and modal representations of  $\mathbf{E}$  and  $\mathbf{H}$ . The fields  $\mathbf{E}$  and  $\mathbf{H}$  are expressed in the cylindrical coordinates  $(\rho, \theta, z)$  as

$$\begin{aligned} \mathbf{E}(\mathbf{r}) &= \rho E_\rho(\mathbf{r}) + \theta E_\theta(\mathbf{r}) + z E_z(\mathbf{r}), \\ \mathbf{H}(\mathbf{r}) &= \rho H_\rho(\mathbf{r}) + \theta H_\theta(\mathbf{r}) + z H_z(\mathbf{r}). \end{aligned} \quad (38)$$

The densities  $\mathbf{M}_s$  and  $\mathbf{J}_s$  are decomposed in the two tangential directions  $\boldsymbol{\tau}$  and  $\boldsymbol{\theta}$ , see Figure 1, as

$$\begin{aligned} \mathbf{M}_s(\mathbf{r}) &= \boldsymbol{\tau} M_\tau(\mathbf{r}) + \boldsymbol{\theta} M_\theta(\mathbf{r}), \\ \mathbf{J}_s(\mathbf{r}) &= \boldsymbol{\tau} J_\tau(\mathbf{r}) + \boldsymbol{\theta} J_\theta(\mathbf{r}). \end{aligned} \quad (39)$$

### 4.1 Fourier series expansions

Let  $g(\mathbf{r})$  represent a surface density or a right hand side and let  $G$  represent an integral operator of Section 3.1 or 3.2 with rotationally invariant kernel  $G(\mathbf{r}, \mathbf{r}')$ . The azimuthal Fourier coefficients  $g_n(r)$  and  $G_n(r, r')$  of the functions  $g(\mathbf{r})$  and  $G(\mathbf{r}, \mathbf{r}')$  are

$$g_n(r) = \frac{1}{\sqrt{2\pi}} \int_{-\pi}^{\pi} e^{-in\theta} g(\mathbf{r}) d\theta, \quad (40)$$

$$G_n(r, r') = \frac{1}{\sqrt{2\pi}} \int_{-\pi}^{\pi} e^{-in(\theta-\theta')} G(\mathbf{r}, \mathbf{r}') d(\theta - \theta'). \quad (41)$$

The azimuthal index  $n$  takes values  $n = 0, \pm 1, \pm 2, \dots$ . Modal integral operators  $G_n$  are defined in terms of the coefficients  $G_n(r, r')$  as

$$G_n g_n(r) = \sqrt{2\pi} \int_{\gamma} G_n(r, r') g_n(r') \rho' d\gamma'. \quad (42)$$

The singularities of  $G(\mathbf{r}, \mathbf{r}')$  are inherited by  $G_n(r, r')$  in the sense that weakly singular operators  $G$  on  $\Gamma$  correspond to weakly singular operators  $G_n$  on  $\gamma$ , and that the same holds for Cauchy-type singular operators.

## 4.2 Modal integral equations

Using (39) and with the notation (40), the Fourier coefficients of the vectors in (26) each gets six scalar entries (transformed scalar surface densities)

$$\boldsymbol{\sigma}_n = \begin{bmatrix} \varrho E_n \\ M_{\tau n} \\ M_{\theta n} \\ J_{\tau n} \\ J_{\theta n} \\ \varrho M_n \end{bmatrix}, \quad \mathbf{f}_{1n} = 2 \begin{bmatrix} E_{1\nu n}^{\text{inc}} \\ E_{1\theta n}^{\text{inc}} \\ -E_{1\tau n}^{\text{inc}} \\ -H_{1\theta n}^{\text{inc}} \\ H_{1\tau n}^{\text{inc}} \\ H_{1\nu n}^{\text{inc}} \end{bmatrix}, \quad \mathbf{f}_{2n} = 2 \begin{bmatrix} m^2 E_{2\nu n}^{\text{inc}} \\ E_{2\theta n}^{\text{inc}} \\ -E_{2\tau n}^{\text{inc}} \\ -H_{2\theta n}^{\text{inc}} \\ H_{2\tau n}^{\text{inc}} \\ H_{2\nu n}^{\text{inc}} \end{bmatrix}. \quad (43)$$

The modal counterpart of (24) and (25) becomes

$$\mathbf{Q}_{1n} \boldsymbol{\sigma}_n = \mathbf{f}_{1n}, \quad (44)$$

$$\mathbf{Q}_{2n} \boldsymbol{\sigma}_n = \mathbf{f}_{2n}. \quad (45)$$

The block operator matrices  $\mathbf{Q}_{1n}$  and  $\mathbf{Q}_{2n}$  can be written

$$\mathbf{Q}_{1n} = \begin{bmatrix} I + 2K_{\nu n} & -2iK_{25n} & 2K_{26n} & -2ikS_{5n} & 2kS_{6n} & 0 \\ -2iK_{12n} & I - K_{1n} & -iK_{2n} & 2kS_{3n} & -2ikS_{4n} & 0 \\ 2K_{24n} & -iK_{3n} & I - K_{4n} & 2ikS_{1n} & -2kS_{2n} & 0 \\ 0 & -2kS_{3n} & 2ikS_{4n} & I - K_{1n} & -iK_{2n} & 2iK_{12n} \\ 0 & -2ikS_{1n} & 2kS_{2n} & -iK_{3n} & I - K_{4n} & -2K_{24n} \\ 0 & -2ikS_{5n} & 2kS_{6n} & 2iK_{25n} & -2K_{26n} & I + 2K_{\nu n} \end{bmatrix} \quad (46)$$

and

$$\mathbf{Q}_{2n} = \begin{bmatrix} I - 2\tilde{K}_{\nu n} & 2im^2\tilde{K}_{25n} & -2m^2\tilde{K}_{26n} & 2im^2k\tilde{S}_{5n} & -2m^2k\tilde{S}_{6n} & 0 \\ 2im^{-2}\tilde{K}_{12n} & I + \tilde{K}_{1n} & i\tilde{K}_{2n} & -2k\tilde{S}_{3n} & 2ik\tilde{S}_{4n} & 0 \\ -2m^{-2}\tilde{K}_{24n} & i\tilde{K}_{3n} & I + \tilde{K}_{4n} & -2ik\tilde{S}_{1n} & 2k\tilde{S}_{2n} & 0 \\ 0 & 2m^2k\tilde{S}_{3n} & -2im^2k\tilde{S}_{4n} & I + \tilde{K}_{1n} & i\tilde{K}_{2n} & -2i\tilde{K}_{12n} \\ 0 & 2im^2k\tilde{S}_{1n} & -2m^2k\tilde{S}_{2n} & i\tilde{K}_{3n} & I + \tilde{K}_{4n} & 2\tilde{K}_{24n} \\ 0 & 2im^2k\tilde{S}_{5n} & -2m^2k\tilde{S}_{6n} & -2i\tilde{K}_{25n} & 2\tilde{K}_{26n} & I - 2\tilde{K}_{\nu n} \end{bmatrix}, \quad (47)$$

where  $I$  is the identity,  $S_{in}$  and  $K_{in}$ , with various indices  $i$ , are modal operators stemming from  $\mathcal{S}$ ,  $\mathcal{N}$ , and  $\mathcal{K}$  and generally defined via (41) and (42),

and the tilde symbol means the replacement of  $k$  by  $k_2$  as explained in Section 3.1. The operators  $S_{in}$  are weakly singular. The  $K_{in}$  are weakly singular for  $i = \nu, 1, 2, 3, 4$  and Cauchy-type singular for  $i = 12, 24, 25, 26$ .

All modal operators in (46) and (47) are detailed in [13, Appendix A] except for  $K_{in}$ ,  $i = 24, 25, 26$ , which are given in Appendix A of the present paper.

### 4.3 Modal representations of $\mathbf{E}$ and $\mathbf{H}$

Once the modal counterpart of (27),

$$(\mathbf{Q}_{1n} + \mathbf{Q}_{2n}) \boldsymbol{\sigma}_n = \mathbf{f}_{1n} + \mathbf{f}_{2n}, \quad (48)$$

has been solved for  $\boldsymbol{\sigma}_n$ , modal representations of  $\mathbf{E}$  and  $\mathbf{H}$  can be constructed from modal counterparts of (17) and (18).

The modal representations of the fields in  $V_1$  are

$$\begin{aligned} E_{\rho n}(r) &= K_{11n} \varrho_{En} - iK_{5n} M_{\tau n} - K_{6n} M_{\theta n} + ikS_{7n} J_{\tau n} + kS_{8n} J_{\theta n}, \\ E_{\theta n}(r) &= iK_{12n} \varrho_{En} - K_{7n} M_{\tau n} - iK_{8n} M_{\theta n} + kS_{9n} J_{\tau n} + ikS_{10n} J_{\theta n}, \\ E_{zn}(r) &= K_{13n} \varrho_{En} - iK_{9n} M_{\tau n} - K_{10n} M_{\theta n} + ikS_{11n} J_{\tau n}, \end{aligned} \quad (49)$$

and

$$\begin{aligned} H_{\rho n}(r) &= ikS_{7n} M_{\tau n} + kS_{8n} M_{\theta n} + iK_{5n} J_{\tau n} + K_{6n} J_{\theta n} + K_{11n} \varrho_{Mn}, \\ H_{\theta n}(r) &= kS_{9n} M_{\tau n} + ikS_{10n} M_{\theta n} + K_{7n} J_{\tau n} + iK_{8n} J_{\theta n} + iK_{12n} \varrho_{Mn}, \\ H_{zn}(r) &= ikS_{11n} M_{\tau n} + iK_{9n} J_{\tau n} + K_{10n} J_{\theta n} + K_{13n} \varrho_{Mn}. \end{aligned} \quad (50)$$

The modal representations of the fields in  $V_2$  are

$$\begin{aligned} E_{\rho n}(r) &= -m^{-2} \tilde{K}_{11n} \varrho_{En} + i\tilde{K}_{5n} M_{\tau n} + \tilde{K}_{6n} M_{\theta n} - ik\tilde{S}_{7n} J_{\tau n} - k\tilde{S}_{8n} J_{\theta n}, \\ E_{\theta n}(r) &= -im^{-2} \tilde{K}_{12n} \varrho_{En} + \tilde{K}_{7n} M_{\tau n} + i\tilde{K}_{8n} M_{\theta n} - k\tilde{S}_{9n} J_{\tau n} - ik\tilde{S}_{10n} J_{\theta n}, \\ E_{zn}(r) &= -m^{-2} \tilde{K}_{13n} \varrho_{En} + i\tilde{K}_{9n} M_{\tau n} + \tilde{K}_{10n} M_{\theta n} - ik\tilde{S}_{11n} J_{\tau n}, \end{aligned} \quad (51)$$

and

$$\begin{aligned} H_{\rho n}(r) &= -im^2 k\tilde{S}_{7n} M_{\tau n} - m^2 k\tilde{S}_{8n} M_{\theta n} - i\tilde{K}_{5n} J_{\tau n} - \tilde{K}_{6n} J_{\theta n} - \tilde{K}_{11n} \varrho_{Mn}, \\ H_{\theta n}(r) &= -m^2 k\tilde{S}_{9n} M_{\tau n} - im^2 k\tilde{S}_{10n} M_{\theta n} - \tilde{K}_{7n} J_{\tau n} - i\tilde{K}_{8n} J_{\theta n} - i\tilde{K}_{12n} \varrho_{Mn}, \\ H_{zn}(r) &= -im^2 k\tilde{S}_{11n} M_{\tau n} - i\tilde{K}_{9n} J_{\tau n} - \tilde{K}_{10n} J_{\theta n} - \tilde{K}_{13n} \varrho_{Mn}. \end{aligned} \quad (52)$$

Here the operators  $S_{in}$  and  $K_{in}$ , with various indices  $i$ , are detailed in [12] and [13, Appendix A].

#### 4.4 Eigenwavenumbers, eigenfields, and fundamental modes

The eigenwavenumbers at a prescribed refractive index  $m$  are wavenumbers  $k$  for which, for some azimuthal index  $n$ , there exist nontrivial solutions  $\boldsymbol{\sigma}_n$  to the homogeneous version of (48)

$$(\mathbf{Q}_{1n} + \mathbf{Q}_{2n}) \boldsymbol{\sigma}_n = \mathbf{0}. \quad (53)$$

Our resonance problem now means finding such numbers  $k$ , corresponding eigendensities  $\boldsymbol{\sigma}_n$ , and eigenfields  $\mathbf{E}_n(\mathbf{r})$ ,  $\mathbf{H}_n(\mathbf{r})$  represented by (49)-(52).

In [13] it was shown how to form the physical time-domain fields  $\mathbf{E}_n(\mathbf{r}, t)$  from the Fourier coefficient vector  $\mathbf{E}_n(r)$ . It was shown that one can let  $E_{\rho n}(r) = E_{\rho(-n)}(r)$ . Then the physical component  $E_{\rho n}(\mathbf{r}, t)$  becomes

$$E_{\rho n}(\mathbf{r}, t) = \frac{1}{2} \Re\{(E_{\rho n}(r)e^{in\theta} + E_{\rho(-n)}(r)e^{-in\theta})e^{i\omega t}\}. \quad (54)$$

Since  $\omega = kc$ , we get

$$\omega \equiv \omega_r - i\alpha = \Re\{k\}c + i\Im\{k\}c, \quad (55)$$

where  $\omega_r$  is the real angular frequency and  $\alpha$  is the attenuation constant. Then

$$E_{\rho n}(\mathbf{r}, t) = \Re\{E_{\rho n}(r)e^{-i\omega_r t}\} \cos n\theta e^{-\alpha t}. \quad (56)$$

This is a standing wave in the azimuthal direction. Also  $E_{zn}(\mathbf{r}, t)$  and  $H_{\theta n}(\mathbf{r}, t)$  are proportional to  $\cos n\theta$  whereas  $E_{\theta n}(\mathbf{r}, t)$ ,  $H_{\rho n}(\mathbf{r}, t)$ , and  $H_{zn}(\mathbf{r}, t)$  are proportional to  $\sin n\theta$ . If one lets  $E_{\rho n}(r) = -E_{\rho(-n)}(r)$ , then  $\cos n\theta$  and  $\sin n\theta$  are exchanged in all components.

It is convenient to introduce the concept of the fundamental mode. The fundamental mode, for a given  $n$ , is the resonance with the smallest value of  $|\Re\{k\}|$ . For large  $n$ , it has properties that distinguishes it from other resonances: Its electric and magnetic fields are confined to a small volume in  $V_2$  and are strongly attenuated in the proximity of that small volume. The exponential growth of the fields, in concordance with (11), is only seen at large distances. The ratio  $\omega_r/\alpha$  is large. Fundamental modes with large  $n$  are whispering gallery modes and are important in optical applications as described in Section 1.

## 5 Powers, energies, and far-fields

There is no inner product under which the eigenfields are orthogonal and it is also impossible to uniquely define a stored energy, a radiated power of an eigenfield, and a normalization. It is, nevertheless, relevant to introduce approximate expressions for these quantities and to define the related Q-factor. We define the stored energy as the electromagnetic energy stored

in  $V_2$  and define the radiated power as the power radiated from  $\Gamma$ . The sharpness, or quality, of these definitions becomes better as  $|\Re\{k\}|/|\Im\{k\}|$  increases.

Assume a single resonance with azimuthal index  $n$  that is excited by an incident field for  $t < 0$  and that there are no incident fields for  $t \geq 0$ . According to (56), the physical eigenfield then oscillates with the angular frequency  $\omega_r$  and attenuates as  $e^{-\alpha t}$  for  $t \geq 0$ . For  $t \geq 0$  we let  $P_{\text{rad}}(t)$  denote the radiated power through  $\Gamma$  averaged over one period  $[t, t + T]$ ,  $P_{\text{diss}}(t)$  the dissipated power averaged over the same period, and  $W(t)$  the stored electromagnetic energy in  $V_2$  at time  $t$ . Conservation of energy and (56) lead to the relations

$$P(t) = P_{\text{rad}}(t) + P_{\text{diss}}(t), \quad (57)$$

$$P_{\text{rad}}(t) = P_{\text{rad}}(0)e^{-2\alpha t}, \quad (58)$$

$$P_{\text{diss}}(t) = P_{\text{diss}}(0)e^{-2\alpha t}, \quad (59)$$

$$W(t) = W(0)e^{-2\alpha t}, \quad (60)$$

$$W(0) \equiv \int_0^\infty P(t) dt = \frac{P_{\text{rad}}(0) + P_{\text{diss}}(0)}{2\alpha}. \quad (61)$$

We use the standard definition of the Q-factor which, with (55), can be written

$$Q \equiv \omega_r \frac{W(t)}{P(t)} = -\frac{\Re\{k\}}{2\Im\{k\}}, \quad (62)$$

and introduce

$$Q_{\text{rad}} = \omega_r \frac{W(t)}{P_{\text{rad}}(t)}, \quad (63)$$

$$Q_{\text{diss}} = \omega_r \frac{W(t)}{P_{\text{diss}}(t)}, \quad (64)$$

so that, from (57) and (62),

$$\frac{1}{Q} = \frac{1}{Q_{\text{rad}}} + \frac{1}{Q_{\text{diss}}}. \quad (65)$$

The radiated power from  $V_2$  equals the real part of the Poynting vector integrated over  $\Gamma$

$$\begin{aligned} P_{\text{rad}}(t) &= \frac{1}{2} \Re \left\{ \int_\gamma \nu \cdot (\mathbf{E}_n(r) \times \mathbf{H}_n^*(r)) \rho d\gamma \right\} e^{-2\alpha t} \\ &= \frac{1}{2} \Re \left\{ \int_\gamma (M_{\theta n}(r) J_{\tau n}^*(r) - M_{\tau n}(r) J_{\theta n}^*(r)) \rho d\gamma \right\} e^{-2\alpha t}. \end{aligned} \quad (66)$$

From Gauss theorem and the Maxwell equations it also follows that

$$P_{\text{rad}}(0) = -P_{\text{diss}}(0) - \Im\{k\} \int_A (|\mathbf{H}_n(r)|^2 + \Re\{m^2\} |\mathbf{E}_n(r)|^2) \rho dA, \quad (67)$$

and due to (61),

$$W(0) = \frac{1}{2c} \int_A (|\mathbf{H}_n(r)|^2 + \Re\{m^2\} |\mathbf{E}_n(r)|^2) \rho \, dA. \quad (68)$$

Apart from a scale factor  $\eta_0$ , see Section 2, the expression (68) is the standard expression for the electromagnetic energy in a volume.

The skin depth

$$\delta = (\Im\{m\} \Re\{k\})^{-1} \quad (69)$$

is a measure of  $\Im\{m\}$ . It is derived from the attenuation of a plane wave that impinges at normal incidence on a lossy half space, but is also a measure of the attenuation of waves in dielectric objects. When

$$\delta \gg \text{diam}(V_2), \quad (70)$$

a number of approximations are valid: The electric and magnetic eigenfields inside  $V_2$  and on  $\Gamma$  are, to a high degree, independent of  $\Im\{m\}$ . It then follows, from (66) and (68), that  $Q_{\text{rad}}$  is independent of  $\Im\{m\}$ . It also holds that

$$Q_{\text{diss}} \approx \frac{\Re\{m\}}{2\Im\{m\}}. \quad (71)$$

The normalized far-field pattern of a mode with azimuthal index  $n$  is the  $\phi$ -dependent function

$$\frac{|\mathbf{F}_n(\phi)|}{\max_{0 \leq \phi \leq \pi} |\mathbf{F}_n(\phi)|}, \quad (72)$$

where  $\mathbf{F}_n(\phi)$  is the Fourier coefficient of  $\mathbf{F}$  in (11), and by that

$$\mathbf{F}_n(\phi) = \lim_{|r| \rightarrow \infty} e^{-ik|r|} |r| \mathbf{E}_n(r). \quad (73)$$

The far-field pattern tells us in what directions the stored energy in  $V_2$  is radiated. By reciprocity it also indicates what direction an incident wave should have in order to excite a resonance. Far-field patterns are included in the numerical examples of Section 7.

## 6 Discretization

The Fourier–Nyström discretization scheme for (53) is adopted from [13]. This section gives a brief overview and describes some modifications that are appropriate when solving (53) at high wavenumbers.

## 6.1 Overview

Let  $G_n$  be a generic modal integral operator of the type encountered in (53) and let  $G_n(r, r')$  and  $G(\mathbf{r}, \mathbf{r}')$  be related to  $G_n$  as in Section 4.1. We split  $G_n(r, r')$  into a smooth and a non-smooth function

$$G_n(r, r') = G_n^{(s)}(r, r') + G_n^{(\text{ns})}(r, r'), \quad (74)$$

where  $G_n^{(s)}(r, r')$  is zero when  $r$  and  $r'$  lie close to each other and  $G_n^{(\text{ns})}(r, r')$  is zero otherwise. We also split  $G(\mathbf{r}, \mathbf{r}')$  analogously. The kernel split (74) corresponds to an operator split  $G_n = G_n^{(s)} + G_n^{(\text{ns})}$ .

The discretization of a  $G_n$  in (42) results in a square matrix whose entries are values of  $G_n(r, r')$ , obtained from  $G(\mathbf{r}, \mathbf{r}')$  via (41), multiplied with suitable quadrature weights. As underlying quadrature rules we use the trapezoidal rule in (41) and 16th-order panel-based Gauss–Legendre quadrature in (42). This is sufficient for the accurate discretization of the  $G_n^{(s)}$ .

The efficient discretization of a  $G_n^{(\text{ns})}$  requires that a number of techniques are activated, all of which are described in detail in [12, 13, 19]. The most important are: evaluation of the integral over  $G^{(\text{ns})}(\mathbf{r}, \mathbf{r}')$  in (41) via factorization and convolution; use of fast discrete Fourier transform techniques and half-integer degree Legendre functions of the second kind [27]

$$\mathfrak{Q}_{n-\frac{1}{2}}(\chi) = \int_{-\pi}^{\pi} \frac{\cos(nt) dt}{\sqrt{8(\chi - \cos(t))}}, \quad (75)$$

with

$$\chi = 1 + \frac{|r - r'|^2}{2\rho\rho'}, \quad (76)$$

to evaluate the Fourier coefficients needed in this convolution; 16th-order accurate product integration for singular integrals on  $\gamma$ , constructed on-the-fly and based on known asymptotics of  $\mathfrak{Q}_{n-\frac{1}{2}}(\chi)$  as  $\chi \rightarrow 1^+$ ; a strategy for when to use forward or backward recursion for the evaluation of  $\mathfrak{Q}_{n-\frac{1}{2}}(\chi)$ ; temporary mesh refinement (upsampling) coupled with temporary increase of the quadrature order on  $\gamma$ .

The discretization of the modal representation of  $\mathbf{E}$  and  $\mathbf{H}$  for  $r \notin \gamma$  in Section 4.3 is done in analogy with the discretization of (53).

## 6.2 Modifications

The discretization of a  $G_n^{(\text{ns})}$  becomes more difficult as  $n$  grows. The domain where the known asymptotics of its kernel is useful becomes narrower and forward recursion for  $\mathfrak{Q}_{n-\frac{1}{2}}(\chi)$  becomes increasingly unstable. In previous work we let each quadrature panel along  $\gamma$  be temporarily divided into at most four subpanels for the resolution of  $\mathfrak{Q}_{n-\frac{1}{2}}(\chi)$  at arguments close to

unity and we used (expensive but stable) backward recursion whenever  $\chi > 1.0005$ . Here we allow up to six subpanels and use backward recursion, as in [28], whenever  $\chi > 1.0001$ .

Eigenwavenumbers are found with Broyden's method, which is one of the simplest and most effective secant updating method for solving nonlinear systems [29]: Let  $\lambda(k)$  be the smallest magnitude eigenvalue of the system matrix in (53) at wavenumber  $k$ . We seek eigenwavenumbers  $k$  as solutions to the system

$$\begin{aligned}\Re\{\lambda(k)\} &= 0, \\ \Im\{\lambda(k)\} &= 0,\end{aligned}\tag{77}$$

where  $\Re\{k\}$  and  $\Im\{k\}$  are considered independent unknowns. For an initial guess  $k$  that is reasonably close to a zero of  $\lambda(k)$ , Broyden's method converges to almost full achievable precision in about ten iterations.

Whispering gallery modes (WGMs) with high indices  $n$  have eigendensities  $\sigma_n$  with numerically discernible support only on those parts of  $\gamma$  that lie farthest away from the  $z$ -axis. We exploit this property to reduce the number of unknowns when discretizing (53) in the search for high-index WGMs.

## 7 Numerical examples

We have implemented our Fourier–Nyström scheme for (53) and (49)–(52) in MATLAB, release 2014a. We use a standard implementation and built-in functions. Our workstation has 64 GB of memory and an Intel Core i7-3930K CPU.

The examples we are about to present share some common features:

- The dielectric object is either the unit sphere or the object in Figure 1 whose generating curve  $\gamma$  has the parameterization

$$r(s) = (1 + 0.25 \cos(5s))(\sin(s), \cos(s)), \quad 0 \leq s \leq \pi. \tag{78}$$

- The refractive index is either  $m = 1.5$  or  $m = 1.5 + 5.5 \cdot 10^{-12}i$ .
- The planar field plots show the absolute values of some of the coefficients  $(H_{\rho n}(r), H_{\theta n}(r), H_{zn}(r))$  and  $(E_{\rho n}(r), E_{\theta n}(r), E_{zn}(r))$ . In each example, all six coefficients are evaluated and scaled with a common factor so that the largest pointwise value of at least one coefficient is unity. The coefficients are evaluated at  $5 \cdot 10^5$  points  $r$  on a Cartesian grid in a rectangle of height 2.6 and width 1.3 and with its left side coinciding with the  $z$ -axis in the half-plane depicted in Figure 1(c). For ease of interpretation, we also show mirror images so that a field plot includes  $10^6$  points in a square of side length 2.6 in the  $xz$ -plane.

- The estimated errors in the field plots are taken as the absolute value of the pointwise difference to a reference solution. In the absence of semi-analytic solutions, the reference solution is obtained with an overresolved mesh containing 50 per cent more quadrature panels on  $\gamma$ . The error plots use a logarithmic scale.

Our examples cover two modal cases, both with high  $k$ : fundamental modes with large  $n$  and a general resonance with a small  $n$ . In addition to finding eigenwavenumbers and showing field plots we also do a convergence study, compute Q-values, and present far-field patterns. The convergence study comprises a comparison between our formulation (53) and a homogeneous modal version of the Müller formulation (31).

## 7.1 The fundamental mode for large $n$

### 7.1.1 The unit sphere

Our first example is the fundamental  $n = 90$  mode of the unit sphere with  $m = 1.5$  and is intended as a verification of the solver. The reference solution is evaluated from a semi-analytic solution given by Mie theory [30]. The eigenwavenumber  $k = 65.09451518155629 - 1.3 \cdot 10^{-13}i$ , found by the solver, corresponds to a sphere diameter of 20.7 vacuum wavelengths and agrees with the value  $k = 65.09451518155630 - 1.3 \cdot 10^{-13}i$ , obtained from the semi-analytic solution, to almost machine precision.

Figure 2 shows field plots of  $(|H_{\rho 90}(r)|, |H_{\theta 90}(r)|, |H_{z 90}(r)|)$  along with estimated absolute pointwise errors, which peak at around  $100\epsilon_{\text{mach}}$ . In passing we mention that our numerical tests revealed the following relations for the fundamental modes of dielectric spheres:

$$E_{\theta n}(r) = iE_{\rho n}(r) = i\frac{z}{\rho}E_{zn}(r), \quad (79)$$

which we then also derived from the semi-analytic solution.

### 7.1.2 Lossless versus lossy object materials

We now look at the fundamental  $n = 90$  mode of the object in Figure 1 and compare converged eigenwavenumbers and eigenfields for two different object materials. The first material is lossless with  $m = 1.5$ . The eigenwavenumber is  $k = 54.72590089140112 - 1.5 \cdot 10^{-13}i$ , corresponding to a generalized object diameter of about 22.8 vacuum wavelengths. The Q-factor (62) is  $Q = 1.8 \cdot 10^{14}$ . The second material is lossy with  $m = 1.5 + 5.5 \cdot 10^{-12}i$  and has  $k = 54.72590089140112 - 1.9803 \cdot 10^{-10}i$ , which corresponds to a skin depth  $\delta \approx 10^{10}$ . The condition (70) is fulfilled and by that  $Q_{\text{rad}}$  is independent of  $\Im\{m\}$  and (71) holds. A comparison of the eigenwavenumbers reveals that  $\Re\{k\}$  is virtually unaffected by the losses. Since  $Q_{\text{rad}} \gg Q_{\text{diss}}$ ,

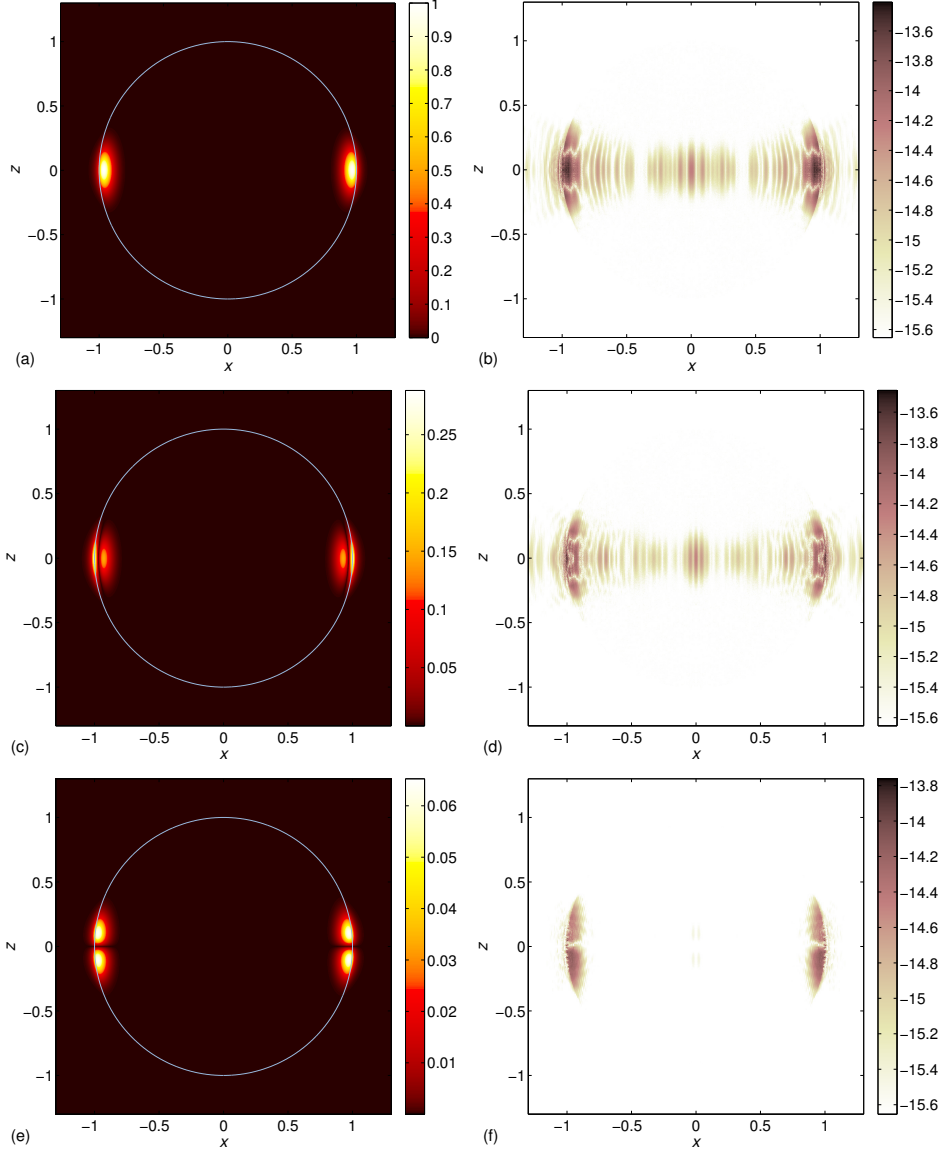


Figure 2: Planar field plots of the magnetic field for the fundamental  $n = 90$  mode of a unit sphere with refractive index  $m = 1.5$ . The eigenwavenumber is  $k = 65.09451518155630 - 1.3 \cdot 10^{-13}i$  and 832 discretization points are used on  $\gamma$ : (a), (c), and (e) show  $|H_{\rho 90}(r)|$ ,  $|H_{\theta 90}(r)|$ , and  $|H_{z 90}(r)|$ ; (b), (d), and (f) show  $\log_{10}$  of the estimated pointwise absolute error.

it follows from (65), (62), and (71) that  $\Im\{k\}/\Re\{k\} \approx -\Im\{m\}/\Re\{m\}$ . Now  $Q = 1.382 \cdot 10^{11}$  and, since the lossless material has  $Q = 1.8 \cdot 10^{14}$ , the dissipative  $Q$ -factor is  $Q_{\text{diss}} = 1.383 \cdot 10^{11}$  according to (65). This value agrees well with the approximate expression  $Q_{\text{diss}} \approx 1.364 \cdot 10^{11}$  from (71).

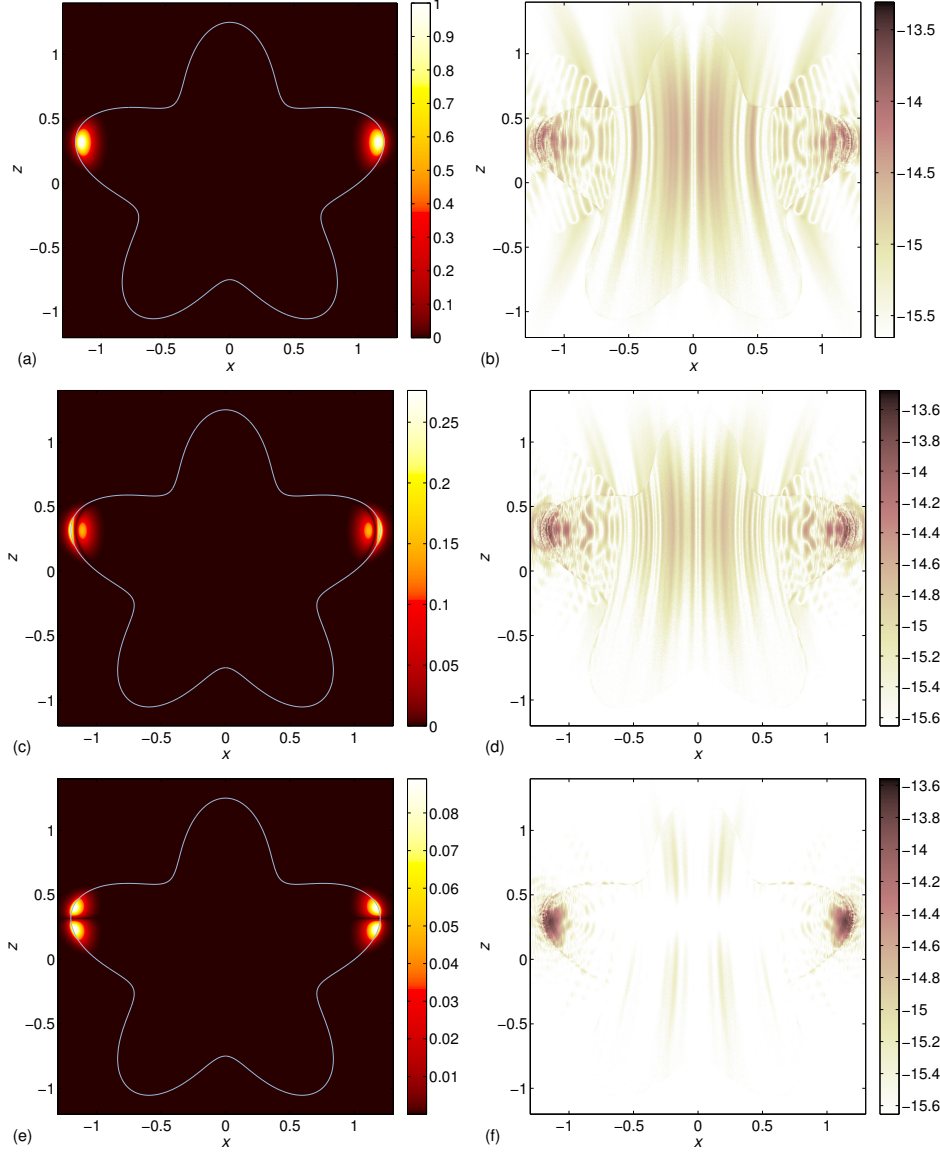


Figure 3: Same as in Figure 2, but for the object in Figure 1 and with  $m = 1.5 + 5.5 \cdot 10^{-12}i$ . The eigenwavenumber is  $k = 54.72590089140112 - 1.9803 \cdot 10^{-10}i$  and 864 discretization points are used on  $\gamma$ .

The losses of the second material is the same as that of silica at the vacuum wavelength of 1550 nm, which is the smallest known loss of any solid material at optical wavelengths. It indicates that the physical limit for the Q-factor is approximately  $10^{11}$ . To the eye, the field plots and the corresponding error plots with the lossless material and with the lossy material are indistinguishable. The images shown in Figure 3 are thus valid

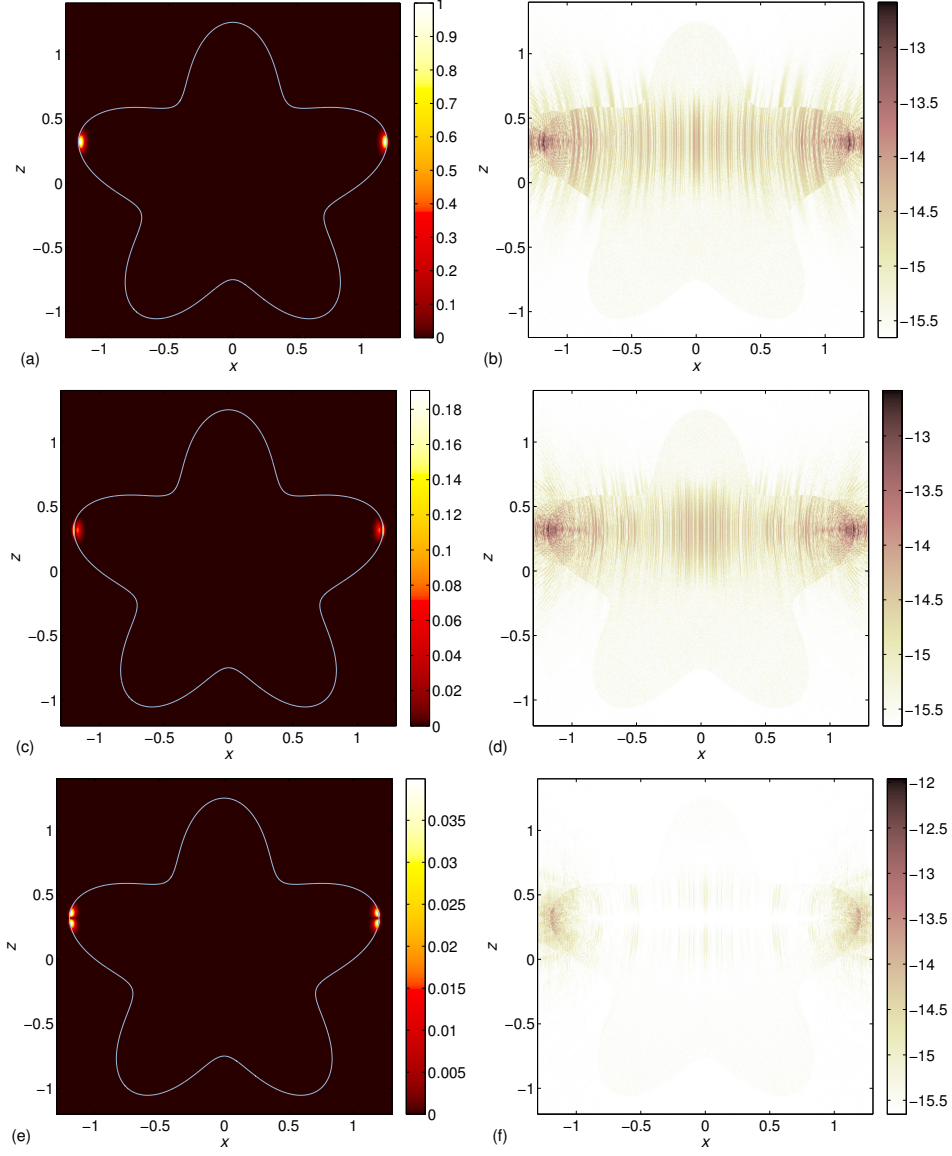


Figure 4: Same as in Figure 3, but for  $n = 450$  and with  $m = 1.5$ . The eigenwavenumber is  $k = 258.059066513439$  and 352 adaptively spaced discretization points are used on  $\gamma$ .

for both object materials. We also tested our scheme for the large loss case with  $m = 1.5 + 5 \cdot 10^{-3}i$ , giving  $k = 54.72532533461791 - 0.17989547170087i$ , without any problem.

### 7.1.3 A high wavenumber WGM

Figure 4 shows planar plots and error estimates of the magnetic field for the fundamental  $n = 450$  mode of the object in Figure 1 with  $m = 1.5$ . The eigenwavenumber of this WGM is  $k = 258.059066513439$ , corresponding to a generalized object diameter of about 107.6 vacuum wavelengths. This is in the regime where asymptotic methods for WGMs are applicable [31]. The imaginary part of  $k$  is not identically zero, but it is too small to be resolved in double precision arithmetic. The images in Figure 4 resemble those of the fundamental  $n = 90$  mode in Figure 3, but with the fields confined to a smaller region and one digit of precision lost. This case has been compared with an evaluation in COMSOL Multiphysics 5.2, which is a FEM simulation package. Since the field is confined to a small region it was possible to reduce the computational domain in COMSOL to a square  $0.25 \times 0.25$ . By that the eigenwavenumber and the eigenfield could be evaluated using default meshes. The convergence of the wavenumber evaluation was of order 1.41. The default mesh referred to as extremely fine used 2557 degrees of freedom and gave the eigenwavenumber 258.1164 with a relative error of  $2.2 \cdot 10^{-4}$ . All of our attempts to analyse other resonances than WGMs with FEM methods failed. This is in contrast to our experience from perfectly conducting cavities, [12] and [13], where FEM is an option also for other resonances.

## 7.2 High $k$ and small $n$

When  $\Im m\{m\} = 0$ , resonances with high  $k$  and small  $n$  have much smaller Q-factors than fundamental modes with similar  $\Re\{k\}$ . We have clearly seen this in numerical test and it can also be understood from a phenomenological description of WGMs in terms of internal reflections. The eigenfields with high  $k$  and small  $n$  vary rapidly both outside and, in particular, inside  $A$  and the problem is harder to resolve.

Figure 5 shows an example for the object in Figure 1 with  $n = 1$  and  $m = 1.5$ . The converged eigenwavenumber  $k = 110.041232211051 - 0.404177078290i$  corresponds to a generalized object diameter of about 45.9 vacuum wavelengths. The large value of  $\Im m\{k\}$  makes the exponential growth of the eigenfields visible already in the object's immediate vicinity.

Figure 6 confirms that our solver exhibits 16th order convergence and is stable under uniform overresolution. The average pointwise accuracy in the field plots saturates at 12–13 digits, which compares favorably with the most accurate results we have found in the literature for general transmission problems involving axially symmetric objects of non-trivial shapes [32].

We have done the same convergence study for our Fourier Nyström scheme applied to (31). The result is given in Figure 7. The convergence order is 15 for (31) compared to 16 for our combination (53). The Müller com-

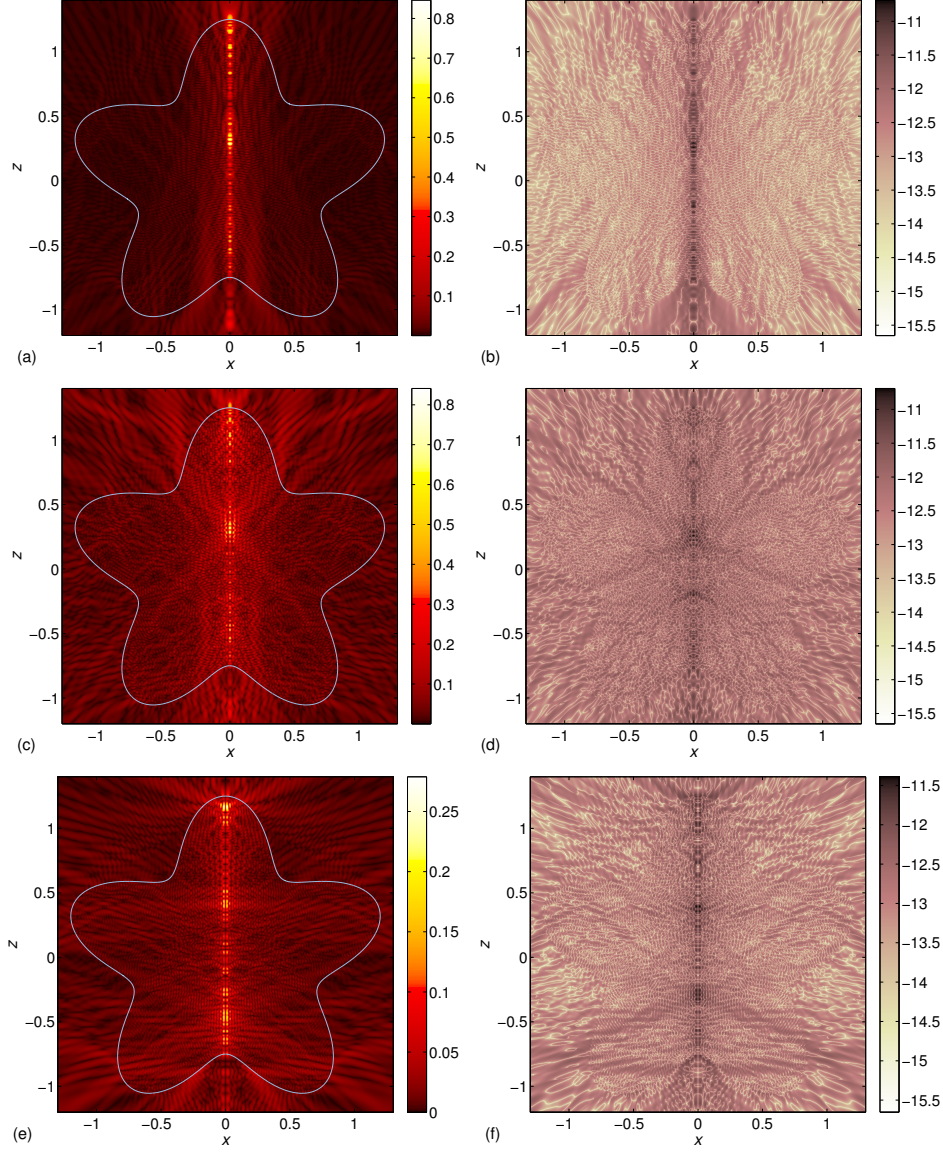


Figure 5: Planar field plots of the electric field for an  $n = 1$  mode of the object in Figure 1. The eigenwavenumber is  $k = 110.041232211051 - 0.404177078290i$ , the refractive index is  $m = 1.5$ , and 1984 discretization points are used on  $\gamma$ : (a), (c), and (e) show  $|E_{\rho 1}(r)|$ ,  $|E_{\theta 1}(r)|$ , and  $|E_{z1}(r)|$ ; (b), (d), and (f) show  $\log_{10}$  of the estimated pointwise absolute error.

bination (31) needs 36 discretization points per vacuum wavelength along  $\gamma$  for saturated convergence, compared to 26 for (53). The relative error of the largest absolute value of the evaluated field components in Figure 5 is  $1.3 \cdot 10^{-12}$  for (31) and  $3.7 \cdot 10^{-13}$  for (53). The construction of the system

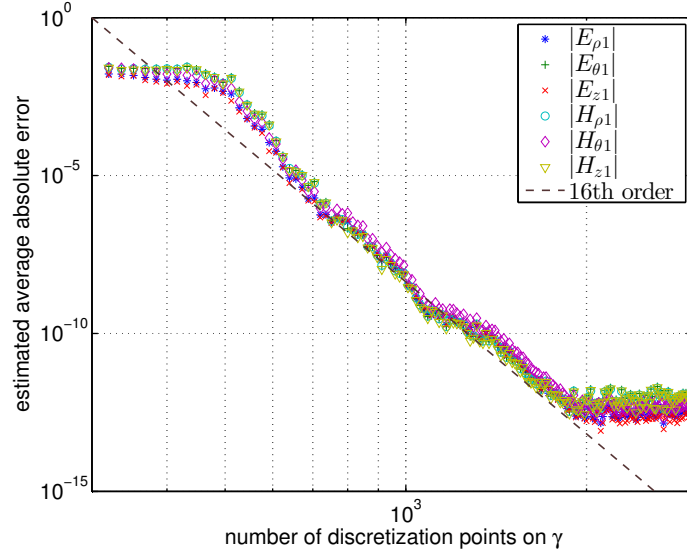


Figure 6: Convergence of the electric field plots shown in Figure 5 and of the corresponding magnetic field. The average pointwise accuracy has converged to between 12 and 13 digits at 1984 discretization points on  $\gamma$ , corresponding to about 26 points per vacuum wavelength along  $\gamma$ .

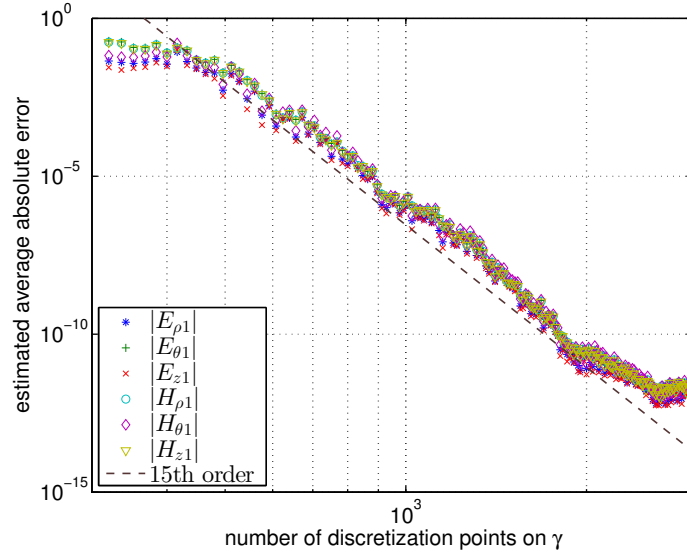


Figure 7: Same as in Figure 6, but based on the Müller combination (31). The average pointwise accuracy has converged to almost 12 digits at 2640 discretization points on  $\gamma$ , corresponding to about 36 points per vacuum wavelength along  $\gamma$ .

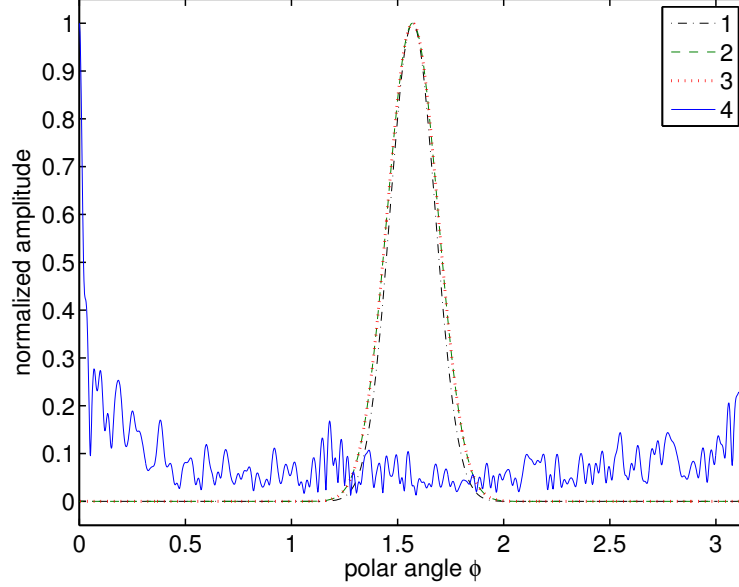


Figure 8: Far-field patterns: curve 1 is for the WGM of the unit sphere of Section 7.1.1; curves 2 and 3, which are almost identical, are for the WGMs with lossless and lossy object materials of Section 7.1.2; curve 4 is for the  $n = 1$  mode of Section 7.2.

matrix took 680 seconds for (31) and 350 seconds for (53). It took 45 seconds to find the solution to (31), compared to 70 seconds for (53). It took on average 0.072 seconds to evaluate the six field components at a point  $r$  for (31) and 0.042 seconds for (53), with (49)–(52).

### 7.3 Far-field patterns

Far-field patterns of resonant modes are defined by (72) and (73). A necessary condition for their meaningful evaluation when  $\Im m\{m\} = 0$  is that  $\Im m\{k\}$  is known with a relative accuracy better than one per cent. This means that if  $Q_{\text{rad}}$ , which for  $\Im m\{m\} = 0$  is equal to  $Q$ , is on the order of  $10^p$ , then  $k$  needs to be resolved with at least  $p + 2$  digits. This condition, coupling the magnitude of  $Q_{\text{rad}}$  to the precision required in  $k$ , seems to hold also when  $\Im m\{m\} \neq 0$ . The requirement of  $p + 2$  accurate digits in  $k$  is met in all our examples, except for that of the high wavenumber WGM in Section 7.1.3.

Figure 8 shows that the far-field patterns of the WGMs are smooth and resemble each other. Their radiated fields peak at the equator,  $\phi = \pi/2$ . The variation in the pattern of the  $n = 1$  mode of Section 7.2 is rapid, as expected.

## 8 Conclusions

Our solver, for the determination of resonant modes of axially symmetric dielectric objects, uses integral equations, related to the Müller formulation, and charge integral equations. This, in combination with a high-order convergent discretization, allows for exceptionally accurate results and excludes the possibility of finding spurious solutions. Moreover, the solver extends the admissible size of objects for which high accuracy can be obtained, based on the full vectorial Maxwell equations, into the regime where asymptotic methods for WGMs are applicable. We stress the following capabilities of our solver up to such object sizes:

- The evaluation of the entire spectrum and all eigenfields with  $\Re\{k\}$  in a given interval. This includes the computationally difficult resonances with small  $n$  and high  $k$ .
- The evaluation of eigenfields at any point in space. This includes slowly-evanescent and radiated fields.
- The evaluation of far-field patterns of WGMs with radiative Q-factors up to  $10^{13}$ .
- Geometric flexibility. While high-order surface information is a prerequisite, non-smooth boundaries can be treated.

These capabilities open up for new studies related to the coupling of electromagnetic waves into WGMs, to finding new object shapes for WGMs and resonances in objects with non-linear as well as active materials. They also make the solver ideal for benchmarking.

## Acknowledgement

This work was supported by the Swedish Research Council under contract 621-2014-5159.

## Appendix A. The operators $K_{24n}$ , $K_{25n}$ , and $K_{26n}$

The modal operators  $K_{in}$ ,  $i = 24, 25, 26$ , are most easily defined in terms of (41) and (42) and the kernels

$$K_i(\mathbf{r}, \mathbf{r}') = D_i(\mathbf{r}, \mathbf{r}')(1 - ik|\mathbf{r} - \mathbf{r}'|)e^{ik|\mathbf{r} - \mathbf{r}'|}, \quad i = 24, 25, 26, \quad (\text{A.1})$$

with static factors

$$D_{24}(\mathbf{r}, \mathbf{r}') = \frac{\boldsymbol{\tau} \cdot (\mathbf{r} - \mathbf{r}')}{4\pi|\mathbf{r} - \mathbf{r}'|^3}, \quad (\text{A.2})$$

$$D_{25}(\mathbf{r}, \mathbf{r}') = i \frac{(\nu_\rho \nu' \cdot \mathbf{r}' + \nu'_z \tau \cdot \mathbf{r}) \sin(\theta - \theta')}{4\pi |\mathbf{r} - \mathbf{r}'|^3}, \quad (\text{A.3})$$

$$D_{26}(\mathbf{r}, \mathbf{r}') = \frac{\nu_z \rho' - (\tau \cdot \mathbf{r} + \nu_\rho z') \cos(\theta - \theta')}{4\pi |\mathbf{r} - \mathbf{r}'|^3}. \quad (\text{A.4})$$

and, with notation as in [13, Appendix A], corresponding Fourier coefficients

$$D_{24n}(r, r') = -\eta \left[ d(\tau) \mathfrak{R}_n(\chi) - \frac{\nu_z}{\rho} \mathfrak{P}_n(\chi) \right], \quad (\text{A.5})$$

$$D_{25n}(r, r') = \eta \frac{(\nu_\rho \nu' \cdot \mathbf{r}' + \nu'_z \tau \cdot \mathbf{r})}{\rho \rho'} n \mathfrak{Q}_{n-\frac{1}{2}}(\chi), \quad (\text{A.6})$$

$$D_{26n}(r, r') = \eta \left[ d(\tau) \mathfrak{R}_n(\chi) + \frac{(\tau \cdot \mathbf{r} + \nu_\rho z')}{\rho \rho'} \mathfrak{P}_n(\chi) \right]. \quad (\text{A.7})$$

The reason for including (A.5)-(A.7) in this exposition is that these expressions are used in the convolutions in our numerical scheme, see Section 6.1.

## References

- [1] A.A. Kishk, Y. Yin, and A.W. Glisson, “Conical dielectric resonator antennas for wide-band applications,” *IEEE Trans. Antennas Propag.*, vol. 50, no. 4, pp. 469–474, Apr. 2002.
- [2] I.M. Reaney and D. Iddles, “Microwave dielectric ceramics for resonators and filters in mobile phone networks,” *J. Am. Ceram. Soc.*, vol. 89, no. 7, pp. 2063–2072, Jul. 2006.
- [3] S.J. Fiedziuszko, I.C. Hunder, T. Itoh, Y. Kobayashi, T. Nishikawa, S.N. Stitzer, and K. Wakino, “Dielectric materials, devices, and circuits,” *IEEE Trans. Microw. Theory Tech.*, vol. 50, no. 3, pp. 706–720, Mar. 2002.
- [4] A.B. Matsko and V.S. Ilchenko, “Optical resonators with whispering gallery modes – part I: basics,” *IEEE J. Sel. Top. Quantum Electron.*, vol. 12, no. 1, pp. 3–14, Jan./Feb. 2006.
- [5] L. He, Ş.K. Özdemir, and L. Yang, “Whispering gallery microcavity lasers,” *Laser Photon. Rev.*, vol. 7, no. 1, pp. 60–82, Jan. 2013.
- [6] M.R. Foreman, J.D. Swaim, and F. Vollmer, “Whispering gallery mode sensors,” *Adv. Opt. Photon.*, vol. 7, no. 2, pp. 168–240, Jun. 2015.
- [7] Y.K. Chembo and N. Yu, “Modal expansion approach to optical-frequency-comb generation with monolithic whispering-gallery-mode resonators,” *Phys. Rev. A*, vol. 82, no. 3, p. 033801, Sep. 2010.
- [8] T.J. Kippenberg, R. Holzwarth, and S.A. Diddams, “Microresonator-based optical frequency combs,” *Science*, vol. 332, no. 6029, pp. 555–559, Jun. 2011.
- [9] R. Ratheesh, M.T. Sebastian, P. Mohanan, M.E. Tobar, J. Hartnett, R. Woode, and D.G. Blair, “Microwave characterisation of BaCe<sub>2</sub>Ti<sub>5</sub>O<sub>15</sub> and Ba<sub>5</sub>Nb<sub>4</sub>O<sub>15</sub> ceramic dielectric resonators using whispering gallery mode method,” *Mater. Lett.*, vol. 45, no. 5, pp. 279–285, Sep. 2000.

- [10] M. Oxborrow, "Traceable 2-D finite-element simulation of the whispering-gallery modes of axisymmetric electromagnetic resonators," *IEEE Trans. Microw. Theory Techn.*, vol. 55, no. 6, pp. 1209–1218, Jun. 2007.
- [11] V.S. Bulygin, Y.V. Gandel, A. Vukovic, T.M. Benson, P. Sewell, and A.I. Nosich, "Nystrom method for the Muller boundary integral equations on a dielectric body of revolution: axially symmetric problem," *IET Microw. Antennas Propag.*, vol. 9, pp. 1186–1192, Aug. 2015.
- [12] J. Helsing and A. Karlsson, "Determination of normalized magnetic eigenfields in microwave cavities," *IEEE Trans. Microw. Theory Techn.*, vol. 63, no. 5, pp. 1457–1467, May 2015.
- [13] J. Helsing and A. Karlsson, "Determination of normalized electric eigenfields in microwave cavities with sharp edges," *J. Comput. Phys.*, vol. 304, pp. 465–486, Jan. 2016.
- [14] V. Amendola, O.M. Bakr, and F. Stellacci, "A study of the surface plasmon resonance of silver nanoparticles by the discrete dipole approximation method: effect of shape, size, structure, and assembly," *Plasmonics*, vol. 5, no. 1, pp. 85–97, Mar. 2010.
- [15] W. Zheng and S. Ström, "The null-field approach to electromagnetic resonance of composite objects," *Comput. Phys. Commun.*, vol. 68, no. 1–3, pp. 157–174, Nov. 1991.
- [16] P. Ylä-Oijala and M. Taskinen, "Well-conditioned Müller formulation for electromagnetic scattering by dielectric objects," *IEEE Trans. Antennas Propag.*, vol. 53, no. 10, pp. 3316–3323, Oct. 2005.
- [17] C. Müller, *Foundations of the Mathematical Theory of Electromagnetic Waves*. Berlin, Germany: Springer-Verlag, 1969.
- [18] H.S. Cohl and J.E. Tohline, "A compact cylindrical Green's function expansion for the solution of potential problems," *Astrophys. J.*, vol. 527, no. 1, pp. 86–101, Dec. 1999.
- [19] J. Helsing and A. Karlsson, "An explicit kernel-split panel-based Nyström scheme for integral equations on axially symmetric surfaces," *J. Comput. Phys.*, vol. 272, pp. 686–703, Sep. 2014.
- [20] J. Helsing and A. Holst, "Variants of an explicit kernel-split panel-based Nyström discretization scheme for Helmholtz boundary value problems," *Adv. Comput. Math.*, vol. 41, no. 3, pp. 691–708, Jun. 2015.
- [21] P. Young, S. Hao, and P.G. Martinsson, "A high-order Nyström discretization scheme for boundary integral equations defined on rotationally symmetric surfaces," *J. Comput. Phys.*, vol. 231, no. 11, pp. 4142–4159, Jun. 2012.
- [22] M. Taskinen and P. Ylä-Oijala, "Current and charge integral equation formulation," *IEEE Trans. Antennas Propag.*, vol. 54, no. 1, pp. 58–67, Jan. 2006.
- [23] F. Vico, Z. Gimbutas, L. Greengard, and M. Ferrando-Bataller, "Overcoming low-frequency breakdown of the magnetic field integral equation," *IEEE Trans. Antennas Propag.*, vol. 61, no. 3, pp. 1285–1290, Mar. 2013.

- [24] M. Ganesh, S.C. Hawkins, and D. Volkov, “An all-frequency weakly-singular surface integral equation for electromagnetism in dielectric media: Reformulation and well-posedness analysis,” *J. Math. Anal. Appl.*, vol. 412, no. 1, pp. 277–300, Apr. 2014.
- [25] D. Colton and R. Kress, *Inverse acoustic and electromagnetic scattering theory*. New York, NY, USA: Springer, 2013, 3rd ed.
- [26] J. Wiersig, “Boundary element method for resonances in dielectric microcavities,” *J. Opt. A: Pure Appl. Opt.*, vol. 5, no. 1, pp. 53–60, Jan. 2003.
- [27] I.S. Gradshteyn and I.M. Ryzhik, *Table of Integrals, Series, and Products*. Amsterdam, the Netherlands: Elsevier, 2007, 7th ed., Eq. 8.713.1.
- [28] A. Gil, J. Segura, and N.M. Temme, *Numerical Methods for Special Functions*. Philadelphia, PA, USA: SIAM, 2007, Remark 3, p. 106.
- [29] M.T. Heath, *Scientific Computing: An introductory survey*. New York, NY, USA: McGraw-Hill, 2002, 2nd ed., p. 241.
- [30] J.A. Stratton, *Electromagnetic Theory*. New York, NY, USA: McGraw-Hill, 1941, p. 615.
- [31] I. Breunig, B. Sturman, F. Sedlmeir, H.G.L. Schwefel, and K. Buse, “Whispering gallery modes at the rim of an axisymmetric optical resonator: Analytical versus numerical description and comparison with experiment,” *Opt. Express*, vol. 21, no. 25, pp. 30683–30692, Dec. 2013.
- [32] Y. Liu and A.H. Barnett, “Efficient numerical solution of acoustic scattering from doubly-periodic arrays of axisymmetric objects,” *J. Comput. Phys.*, vol. 324, pp. 226–245, Nov. 2016.